

## Supplementary Information

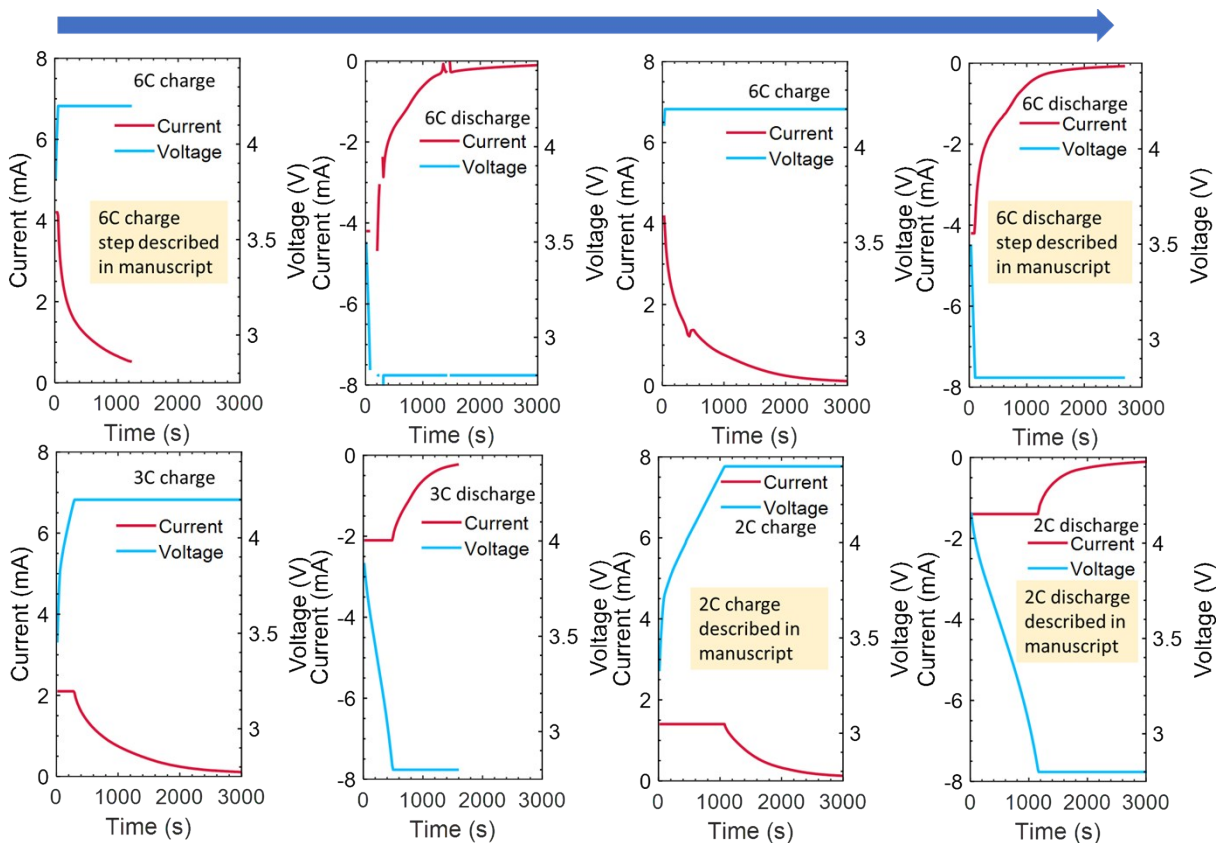
### Operando spatial quantification of lithiation and lithium plating during high-rate operation of graphite electrodes

#### 1. Cycling data

Following formation cycles, the cycling sequence of the operando cell during beam exposure was:

1. 6C charge and 6C discharge between 2.8 V and 4.2 V
2. 6C charge and 6C discharge between 2.8 V and 4.2 V
3. 3C charge and 3C discharge between 2.8 V and 4.2 V
4. 2C charge and 2C discharge between 2.8 V and 4.4 V

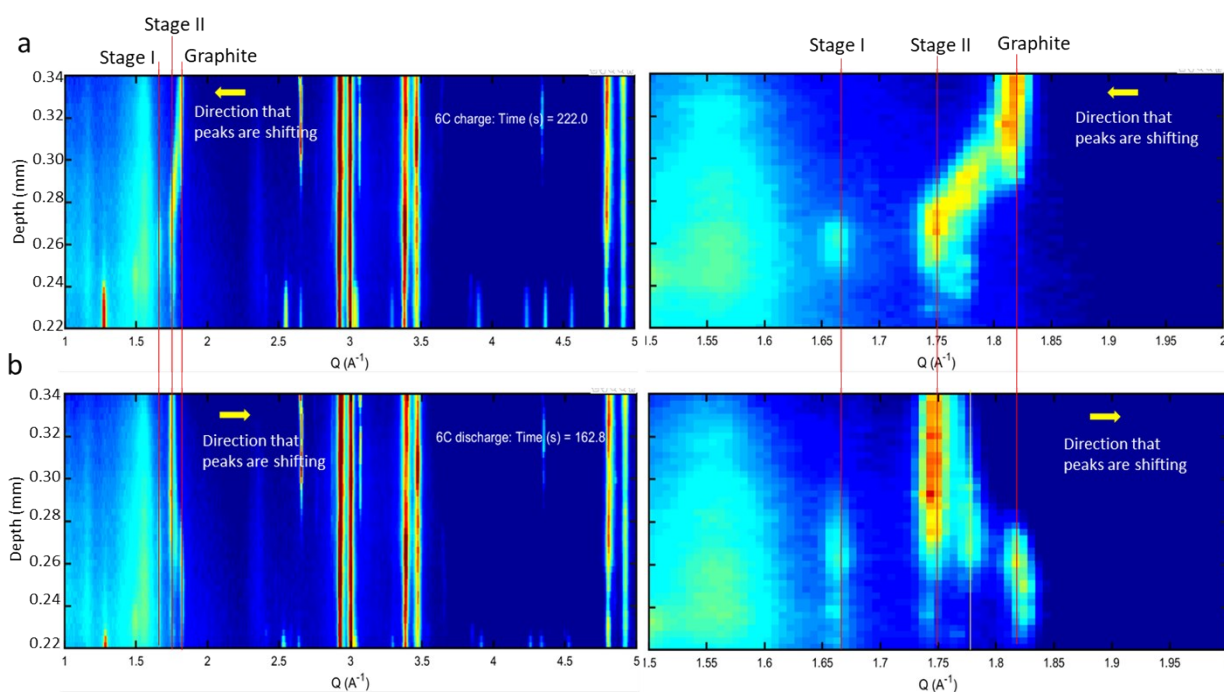
All constant current steps were followed by a constant voltage step. The current and voltage data for all cycles are shown in the following figure. Systematic issues occurred during the first discharge and second charge, so the first 6C charge and second 6C discharge were used to represent the 6C step in the manuscript. The final 2C cycle was also used in the manuscript.



Supplementary Figure 1. Sequentially from left to right, current and voltage profiles of all cycles of the operando-cell. The 6C and 2C charge and discharge steps that were discussed in the manuscript are labelled.

## 2. XRD data showing the hysteresis between charge and discharge

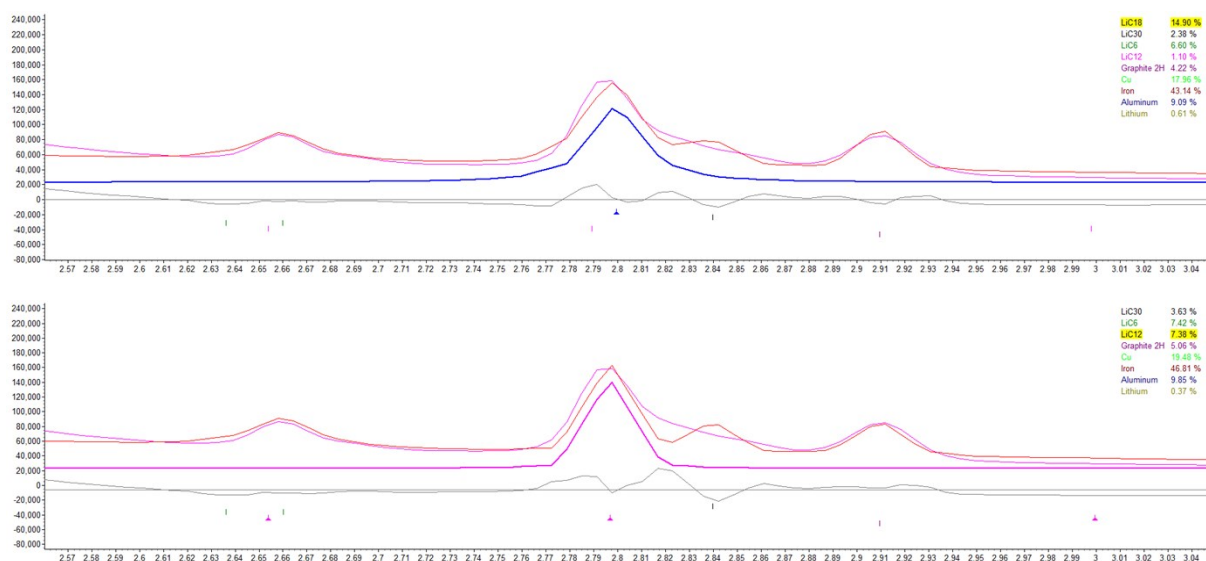
Evidence of hysteresis was observed in the diffraction data between charge and discharge. As shown in the following figure, the characteristic shift in the peak during the transition between graphite and Stage II was different between charge and discharge. During the charge step in the following figure, there was a continuous shift from graphite to Stage II, but during discharge there appeared to be an intermediate peak (indicted with a yellow line) without any continuity. The following figure also highlights the challenge in identifying and quantifying non-equilibrium intermediate phases and compositions with high accuracy using X-ray diffraction.



Supplementary Figure 2. Diffraction peaks plotted for  $Q$  (x-axis) as a function the depth in absolute stage position values (y-axis) showing a wide field (left) and magnified (right) view of the graphite lithiation peaks for (a) 6C charge and (b) 6C discharge. The red lines indicate the  $Q$  values that are characteristic of the labelled stages. A more distinct intermediate peak was observed during discharge (yellow line). Supplementary Movie 1 shows the time-resolved data of these plots.

### 3. Rietveld refinement and XRD data processing

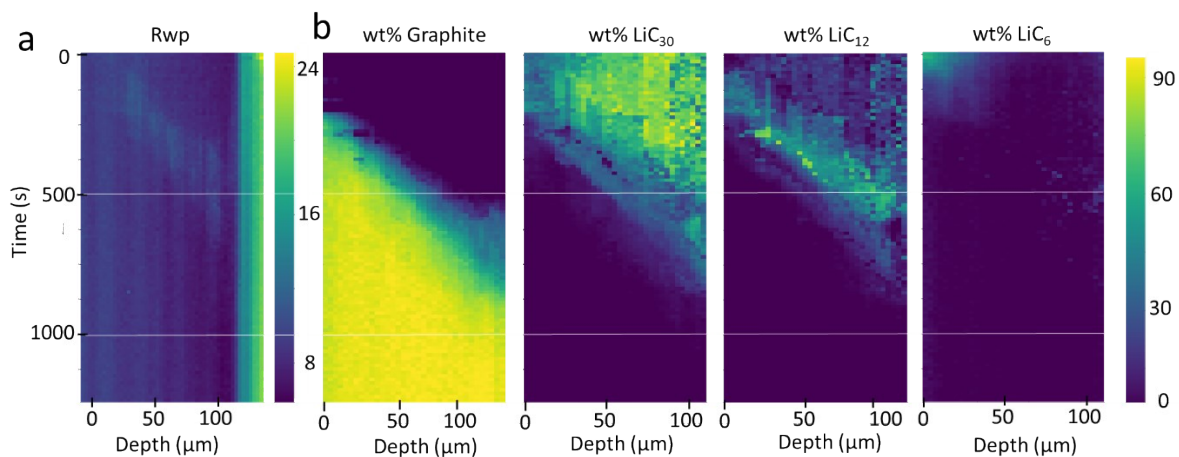
Diffraction data were collected with a wavelength of 0.17196 Å on a Pilatus CdTe photon counting area detector and were integrated with PyFai to give powder diffraction patterns with a step size of 0.00635°. The  $\text{Li}_x\text{C}$  phases present in the powder X-ray diffraction (PXRD) data were initially identified from a diffraction pattern produced by summing all the time and space data in the anode region for the first discharge. This pattern was also used to mask areas containing peaks from the cell casing, current collectors and separator- these regions were omitted from the final Rietveld analysis. Rietveld fits on the summed patterns allowed us to identify peaks from graphite,  $\text{LiC}_6$ ,  $\text{LiC}_{12}$  and  $\text{LiC}_{30}$ . The peaks from  $\text{LiC}_{12}$  and  $\text{LiC}_{18}$  phases described by Missyul et al.<sup>1</sup> could not be distinguished from one another partly because of the low resolution inherent from the experiment geometry but mainly as their peaks overlapped completely in the regions where graphite peaks were visible in our data, as seen in the following figure.



Supplementary Figure 3. Rietveld fits with  $\text{LiC}_{18}$  (top) and  $\text{LiC}_{12}$  (bottom). The pink line is the data for charge step 2 summed over all time and space, showing all the phases observed during charge. Red is the Rietveld fit. Grey is the difference between the observed and fitted curves. In the top plot the blue line is the isolated contribution from  $\text{LiC}_{18}$ . In the bottom plot the purple line shows the isolated contribution from  $\text{LiC}_{12}$ .

The diffraction patterns for individual points in time and space were fitted using surface Rietveld methods in TOPAS V5. A fundamental parameters peak shape was used. It was not possible to fit all the patterns in the anode region for each charge or discharge dataset simultaneously (too many least squares parameters), so they were split into strips which were refined sequentially using a batch method.

Refinements were repeated using data strips of one time for all points in space and all time for one point in space to confirm that there were no artefacts in the refinement caused by the order or grouping of the powder patterns. The refinements used a  $2\theta$  range of  $1 - 8.85^\circ$  with excluded regions from  $4.13 - 5.69$ ,  $6.73 - 7.93$ ,  $8.05 - 8.21$  and  $10.44 - 11.17^\circ$  to mask out signals from the cell casing and current collector (note: it was possible to fit these peaks with copper and iron phases, but this had no significant effect on the graphite fit results compared to masking in fits against the time and space summed data, so the simpler masking approach was used for the main fits). In each diffraction pattern the background was fitted with a 3-term Chebyshev polynomial and two broad peaks (fixed positions, refined intensity and Lorentzian crystallite size broadening terms) were used to fit some broad features probably caused by scattering from the electrolyte and binder. The lattice parameters ( $a$  and  $c$ ), Gaussian crystallite size broadening, and scale were refined for  $\text{Li}_x\text{C}$  phases. Thermal parameters (Biso fixed to 1 for all atoms) and atom positions were not refined. The zero error was fixed at zero. A total of 23 parameters were refined for each diffraction pattern. Rwp variations are not related to the phase distributions as seen in the following figure. Errors were determined using the bootstrap method<sup>2, 3</sup>.

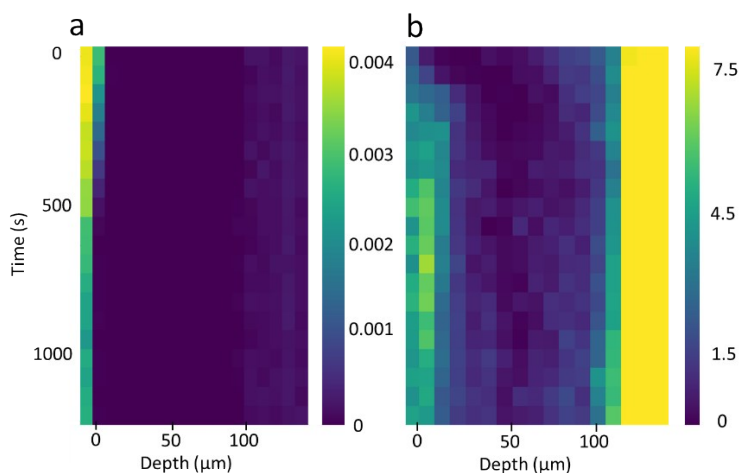


Supplementary figure 4. Time-space heat maps of the graphite anode during the 6C discharge showing (a) the Rwp values and (b) weight percent's of the different phases.

In order to determine the weight percentage of metallic Li close to the spacer we had to sum the data from blocks of diffraction patterns (5 time points by 3 height points) together to obtain diffraction patterns with lower space/time resolution but, more importantly, lower background noise. The peak for Li metal at  $3.97^\circ$  could now be distinguished. The background fitting was much more crucial in these refinements due to the very low weight percentage of Li metal. The  $2\theta$  fitting range was reduced to  $2.5$

– 4 °, covering the strongest peaks for the Li and  $\text{Li}_x\text{C}$  phases and avoiding the low angle electrolyte/binder peaks which can strongly affect the background if poorly fitted. An 11-term Chebyshev polynomial background was used. The same parameters were refined for the  $\text{Li}_x\text{C}$  phases as in the fully time and space resolved fit. For Li metal the weak signal demanded a more complex approach. The cubic lattice parameter and scale were refined with strict limits on the lattice parameter (3.499 - 3.52 Å) and fixed Gaussian crystallite size broadening. To avoid local minima a Monte Carlo approach was used to randomize the starting values of the lattice parameters (random value between 3.5 and 3.51 Å) over multiple cycles of refinement (with the “continue\_after\_convergence” command in TOPAS). The refinements treated all the block summed diffraction patterns for each charge or discharge dataset simultaneously as a single data surface.

The polyethylene in the separator, which is located close to the graphite/electrolyte interface where the Li plating occurs, can also produce a small Bragg peak in the region of the diffraction pattern where the Li peak is observed<sup>4</sup>. To be certain that this was not responsible for the signal we fitted the intensity of the strongest peak from the polymer at  $2-\Theta = 2.39^\circ$  ( $q = 1.5 \text{ \AA}^{-1}$ ) using TOPAS. The intensity variation during charge and discharge is clearly different to that for the lithium peak, as seen in the following figure.



Supplementary Figure 5. Time and space heat map images of the graphite electrode region for charge 2 showing, left: intensity variation in time and space for the polyethylene peak at  $2-\Theta = 2.39^\circ$ , and right: weight % of lithium determined by the Rietveld method.

## 4. Equations used for lithiation quantifications

### Variable parameters

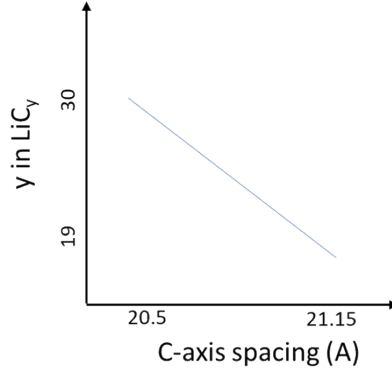
$x$	$x$ in $\text{Li}_x\text{C}_6$	$M_{i,local}$	Mass of phase $i$ at a depth
$f_i$	Mass fraction of lithium in phase $i$	$t$	Time (s)
$m_i$	Mass fraction of phase $i$	$I$	Current (A)
$MW_i$	Molecular weight of phase $i$	$I_{local}$	Local current at a depth (A)
$n_i$	Moles of phase $i$	$I_{density}$	Current density (A/g)
$M_i$	Mass of phase $i$		

### Fixed parameters and values

$\rho_{gr,areal}$	Areal density of graphite	0.01397 g/cm <sup>2</sup>	$A_{gr}$	Area of graphite electrode	0.124 cm <sup>2</sup>
$\rho_{gr}$	Density of graphite	1.38 g/cm <sup>3</sup>	$m_{gr,elec}$	Mass of graphite electrode	0.00173 g
$h_{gr}$	Height of graphite electrode	101 $\mu\text{m}$	$C_{sp,Li}$	Specific capacity of Li	3860 mAh/g
$A_{sp,gr}$	Specific surface area graphite	0.89 m <sup>2</sup> /g	$C_{sp,Gr}$	Specific capacity of graphite	372 mAh/g
$F$	Faraday's constant	96485.3 C/mol	$C_{cell}$	Capacity of operando cell	

### Calculating $x$ in $\text{Li}_x\text{C}_6$ and capacity from XRD data

To calculate the lithiation state  $x$  in  $\text{Li}_x\text{C}_6$ , i.e. the number of moles of Li per mole of  $\text{C}_6$ , from the mass fractions of stages determined from XRD, compositions were assigned to the mass fractions of each phase determined by Rietveld refinement ( $m_{stageI}$ ,  $m_{stageII/III}$ ,  $m_{stageIII}$ ). The stages that were quantified were graphite, Stage III, Stage II/III, and Stage I. As described in the manuscript, the composition of  $\text{LiC}_{12}$  was assigned to Stage II/III and a composition linear to the refined  $c$  cell parameter was assigned to Stage III since its composition is not precisely known. Stage III is considered as a solid solution phase due to the continuous shift in spacing observed with XRD (no phase separation). Hence, we decided not to attach a single composition but instead we used a range of  $x$  that was linked to the  $c$ -axis spacing measured for fitted  $\text{LiC}_{30}$  phase:



Supplementary Figure 6. A linear estimation was made for Stage III between compositions  $\text{LiC}_{30}$  and  $\text{LiC}_{19}$  that spanned the range of c-axis spacings observed for the Stage III refinement fit.

Hence, the following compositions were used for each phase:

1. Graphite:  $\text{C}_6$
2. Stage III: Linear composition with c-axis spacing shown in Supplementary Figure 6
3. Stage II/III:  $\text{LiC}_{12}$
4. Stage I:  $\text{LiC}_6$

Using these compositions, the lithiation state  $x$  in  $\text{Li}_x\text{C}_6$  was calculated from the XRD-determined mass fractions using the following equation:

$$x = 6 \left( \frac{f_{\text{StageIII}} \times m_{\text{StageIII}} + f_{\text{StageII}} \times m_{\text{StageII}} + f_{\text{StageI}} \times m_{\text{StageI}}}{MW_{\text{Li}}} \right) \left( \frac{m_{\text{graphite}} + m_{\text{StageIII}}(1 - f_{\text{StageIII}}) + m_{\text{StageII}}(1 - f_{\text{StageII}}) + m_{\text{StageI}}(1 - f_{\text{StageI}})}{MW_{\text{C}}} \right) \quad \text{S1}$$

To calculate the capacity (Ah) from the XRD measurements ( $\text{Capacity}_{\text{XRD}}$ ) as shown in Figure 1 of the main manuscript, we first calculated the mass of graphite in the system from the electrode parameters provided by the CAMP manufacturing facility at Argonne National Laboratory (see Fixed parameters above), and then determined the cell's theoretical capacity using the specific energy density of graphite. The  $\text{Capacity}_{\text{XRD}}$  was then calculated as a fraction of the cell's capacity, i.e. the lithiation state  $x$  in  $\text{Li}_x\text{C}_6$  was applied as a factor.

$$M_{\text{gr}} = A_{\text{gr}} \rho_{\text{gr. areal}} \quad \text{S2}$$

$$C_{\text{cell}} = C_{\text{sp.Gr}} M_{\text{gr}} \quad \text{S3}$$

$$\text{Capacity}_{\text{XRD}} = x C_{\text{cell}} \quad \text{S4}$$

### Current and current density estimation from XRD data

The current necessary to change the electrode's lithiation state,  $x$  in  $\text{Li}_x\text{C}_6$ , was calculated using Faraday's constant ( $F$ ):

$$I = \frac{\Delta x F M_{gr}}{\Delta t MW_{C6}} \quad \text{S5}$$

The current density values for the plots shown in Figure 6 of the main manuscript were determined by calculating the current for each slice ( $I_{local}$ ) and dividing by the surface area of graphite estimated to be within the depth-window of measurement.

$$I_{density} = \frac{I_{local}}{A_{sp.gr} M_{gr.local}} \quad \text{S6}$$

This estimation assumes that each window of depth contains the same specific surface area and mass of graphite, i.e. homogeneous material properties and distribution of graphite within the electrode.

### Percent capacity of Li plating

To calculate the mass of plated Li and the percent of the cell's capacity to which it amounted, the total mass of lithiated graphite ( $M_{lithiated}$ ), which includes the mass of graphite and lithium, was first determined. Here  $m_{gr} + m_{StageIII} + m_{StageII} + m_{StageI} + m_{Li} = 1$ .

$$M_{lithiated} = \left( \frac{M_{C6}}{1 - m_{Li} - m_{LiC30} \frac{MW_{Li}}{MW_{LiC30}} - m_{LiC12} \frac{MW_{Li}}{MW_{LiC12}} - m_{LiC6} \frac{MW_{Li}}{MW_{LiC6}}} \right) \quad \text{S7}$$

The mass of plated Li ( $M_{Li}$ ) was then calculated using the mass fraction of Li plating.

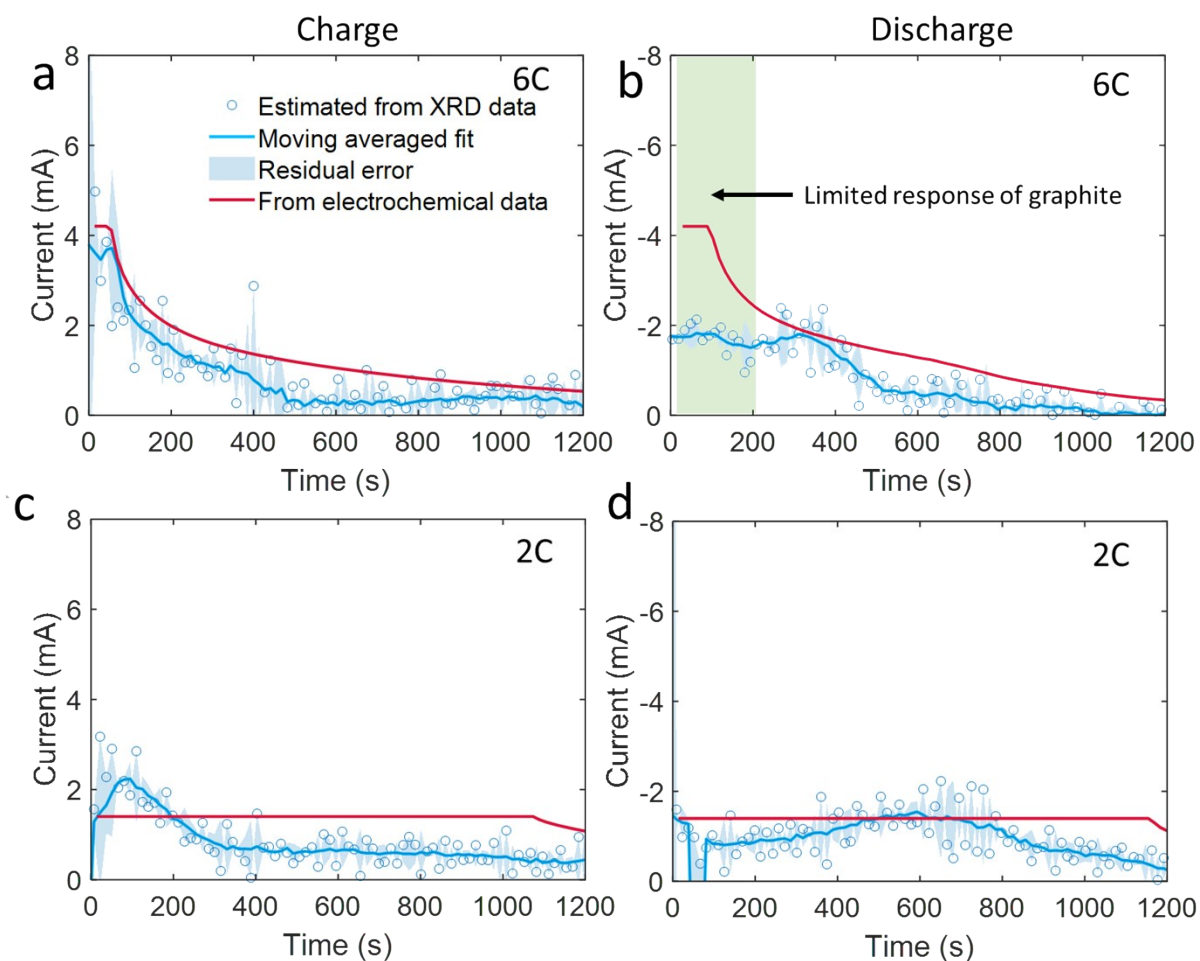
$$M_{Li} = (M_{lithiated})(m_{Li}) \quad \text{S8}$$

Finally, the capacity of the plated Li was determined using the specific capacity of Li ( $C_{sp,Li}$ ) and the capacity of the operando cell ( $C_{cell}$ ).

$$Capacity\% = \frac{(C_{sp.Li})(M_{Li})}{C_{cell}}(100)$$

## 5. Comparing potentiostat current and current estimated from XRD data

By measuring the summed  $x$  in  $Li_xC_6$  across all depths for each time period, and quantifying the change in  $x$  in  $Li_xC_6$  between consecutive time periods, an estimation of the current that directly lithiates the graphite was made. The estimated current from the XRD data is plotted alongside the current measured potentiostat electrochemical data in the figure below. In general, the current estimated from the XRD data is lower than the potentiostat data which indicates that side-reactions were occurring during the operando measurements. There may have also been some beam-induced degradation reactions too. A major divergence from the potentiostat data occurs at the beginning of the 6 discharge. This is discussed in the main manuscript, and is suspected to have occurred due to corrosion or other side reactions being more thermodynamically favorable at the high applied overpotential during that time than delithiation of the graphite.



Supplementary Figure 6: Comparison between the current measured on the potentiostat electrochemical data and the current estimated from the XRD data for (a) 6C charge, (b) 6C discharge, (c) 2C charge, and (d) 2C discharge.

## 6. Cell performance comparison for increasing rate and electrode thickness

### Properties of electrodes used for comparison

2032 format coin cells were constructed with 16 mm diameter negative electrodes and 14 mm diameter positive electrodes that were soaked in electrolyte consisting of 1.2 MM LiPF<sub>6</sub> in EC:EMC (3:7) with a Celgard 2320 polymer separator. Two electrode types were compared, thick and medium. Both types of electrodes were manufactured at the Cell Analysis, Modeling and Prototyping (CAMP) facility at Argonne National Laboratory and are described below. The cells were initially formed during 2 cycles at a constant current of C/10 between 3.0 V and 4.1 V at which a constant voltage was held until the current reached C/20. This was followed by 2 cycles at C/2 constant current between 3.0 V and 4.1 V at which a constant

voltage was held until the current reached C/20. The cells were then cycled under fast charge conditions that consisted of 6C constant current charge from 3.0 V to 4.1 V followed by constant voltage to C/5. Discharge was carried out at C/2. Every 250 cycles, 3 C/10 cycles were carried out to monitor the capacity of the cell. For comparison, additional cells were operated within the same voltage window at lower rates of 1C charge with constant voltage to C/10 and C/2 discharge.

**Thick electrodes:** High-energy density electrodes were selected for this investigation. The positive electrode consisted of 90 wt% ECOPRO  $\text{LiNi}_{0.6}\text{Mn}_{0.2}\text{Co}_{0.2}\text{O}_2$  (NMC622) with 5 wt% Timcal C45 and 5 wt% Solvay 5130 PVDF. In its dry state, the coating thickness was 112  $\mu\text{m}$  on a 20  $\mu\text{m}$  thick aluminum foil. The coating loading was 30.24  $\text{mg}/\text{cm}^2$  with a density of 2.70  $\text{g}/\text{cm}^3$  and a porosity of 34 %. The areal capacity of the electrode was 4.60  $\text{mAh}/\text{cm}^2$ . The diameters for particle size distribution were D10 = 8.4  $\mu\text{m}$ , D50 = 11.0  $\mu\text{m}$ , and D90 = 14.4  $\mu\text{m}$ . The negative electrode consisted of 91.83 wt% Superior graphite SLC1520P with 2 wt% Timcal C45, 6 wt% Kureha 9300 PVDF Binder, and 0.17 wt% oxalic acid. In its dry state, the coating thickness was 101  $\mu\text{m}$  on a 15  $\mu\text{m}$  thick copper foil. The coating loading was 13.97  $\text{mg}/\text{cm}^2$  with a density of 1.38  $\text{g}/\text{cm}^3$  and porosity of 36.2%. The diameters for particle size distribution were D10 = 11.03  $\mu\text{m}$ , D50 = 16.94  $\mu\text{m}$ , and D90 = 26.76  $\mu\text{m}$ .

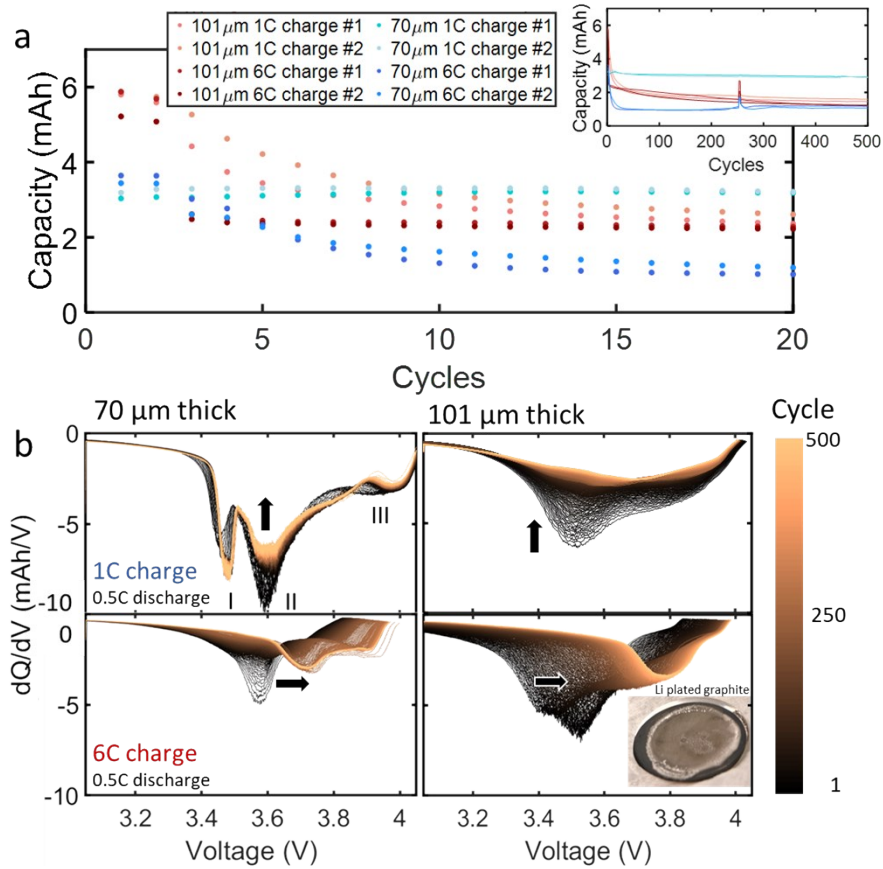
**Medium electrodes:** The positive electrode consisted of 90 wt% Toda NMC532 with 5 wt% Timcal C45 and 5 wt% Solvay 5130 PVDF. In its dry state, the coating thickness was 71  $\mu\text{m}$  on a 20  $\mu\text{m}$  thick aluminum foil. The coating loading was 18.63  $\text{mg}/\text{cm}^2$  with a density of 2.62  $\text{g}/\text{cm}^3$  and a porosity of 35.4 %. The areal capacity of the cathode was 2.5  $\text{mAh}/\text{cm}^2$  based on 4.1 v charge cutoff. The negative electrode consisted of 91.83 wt% Superior graphite SLC1506P with 2 wt% Timcal C45, 6 wt% Kureha 9300 PVDF Binder and 0.17 wt% oxalic acid. In its dry state, the coating thickness was 70  $\mu\text{m}$  on a 10  $\mu\text{m}$  thick copper foil. The coating loading was 9.94  $\text{mg}/\text{cm}^2$  with a density of 1.42  $\text{g}/\text{cm}^3$  and porosity of 34.5 %.

### Results of cycling

The capacity fade of the cells is shown in Supplementary Figure 7a, where the first two cycles were at C/10 constant current charge and discharge, and a constant voltage hold after the charge step to C/20, thus capturing the original capacity of the cell. The rate of capacity fade was most severe for the 101  $\mu\text{m}$  electrodes, and for both the 101  $\mu\text{m}$  and 70  $\mu\text{m}$  electrodes the fast charge cycles exhibited the greatest rate of capacity fade.

Differential capacity analysis during cycling can provide some insight into the degradation mechanisms and limitations of cells<sup>5, 6</sup>. The discharge  $dQ.dV^{-1}$  for the 70  $\mu\text{m}$  and 101  $\mu\text{m}$  electrodes during fast and normal charge conditions are shown in Supplementary Figure 7(b,c). Peaks I, II and III for the 70  $\mu\text{m}$  electrode exposed to 1C charge conditions in Supplementary Figure 7b were primarily associated with the different stages of graphite lithiation but are also influenced by the transitions of NMC. The reduction in peak II and III, but not peak I, indicates that side reactions reducing lithium ions (e.g. through SEI formation) was a prominent cause of capacity loss. If it was loss of active material in the negative electrode, all three peaks would have diminished. Following 6C charging, the peaks broadened and diminished for the 70  $\mu\text{m}$  electrode. Peak broadening may indicate that phase transitions occurred over a wider range of applied voltage, which may have been caused by lithium concentration gradients where a front of phase transitions progressed further into the electrode while the applied voltage continued to change. The travelling front of phase change would have been observed as a change in Q for a wider range of V. The increase in discharge capacity accessed at higher potentials, along with the flattening of the  $dQ.dV^{-1}$  profile after about 20 cycles, is not characteristic behavior of graphite suggesting that the graphite was not being accessed. This might indicate that Li stripping is occurring, and its reversible nature then takes over as the main charge transfer mechanism. However, there may also be some affect from degradation at the positive electrode.

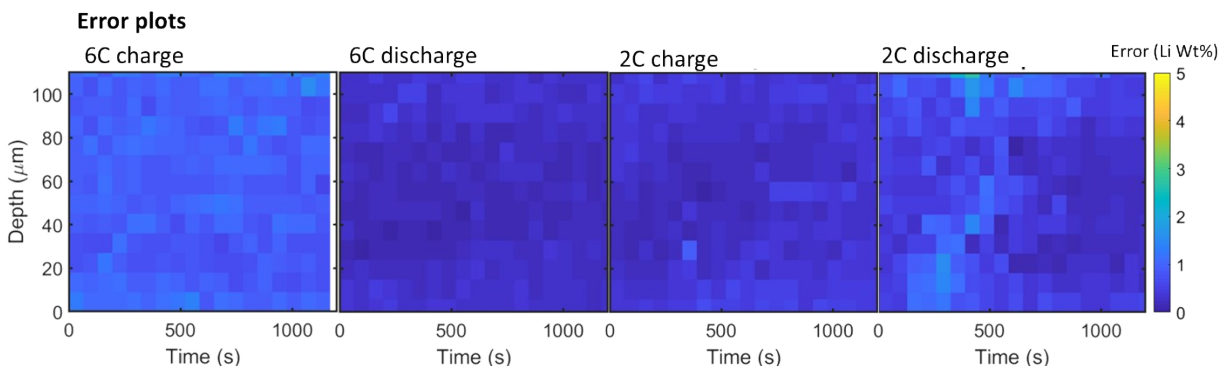
For the 101  $\mu\text{m}$  electrode, the  $dQ.dV^{-1}$  profiles deviated immediately from the ideal cell profile, as shown in Supplementary Figure 7. For the 101  $\mu\text{m}$  electrode charged at 1C (top in Supplementary Figure 7b) extreme peak broadening occurred initially, and the profile flattened during cycling. The peak broadening was severe and likely due to the front of phase change travelling through the electrode like before, and the loss of capacity likely stemmed from loss of Li inventory rather than degradation of the active material. For the 101  $\mu\text{m}$  electrode subject to 6C charge conditions (bottom in Supplementary Figure 7b), broad peaks also existed initially and there was an overall shift of the peaks to a higher voltage. Similarly, under 1C charge conditions, severe lithiation heterogeneities are expected to have been present during fast charge. The shift of the  $dQ.dV^{-1}$  towards higher voltages indicates an increased deviation from the behavior of graphite and an increased role of Li plating in the charge transfer process where the Q would increasingly come from the plated Li rather than the graphite. Li plating was confirmed upon disassembly. However, some postmortem analysis, modelling, and depth-profiling experiments are needed to confirm these hypotheses.



Supplementary Figure 7. (a) Discharge capacity during cycling of cells with 70  $\mu\text{m}$  (blue) and 101  $\mu\text{m}$  (red) thick negative electrodes during 1C (light color) and 6C (dark color) charge conditions. (b) C/2 discharge  $dQ \cdot dV^{-1}$  plots for 70  $\mu\text{m}$  (left) and 101  $\mu\text{m}$  (right) thick negative electrodes exposed to 1C charge (top) and 6C charge (bottom) conditions. Arrows indicate the direction of peak shift.

## 7. Li plating errors

The error values for the mass fractions of Li quantified for each of the charge and discharge steps in the main manuscript are presented in the following figure. The error is typically around 1% or a mass fraction of 0.01 for each measurement.



Supplementary Figure 8. Error values for the mass fractions of Li quantified for each charge and discharge described in the manuscript.

## 8. Electrochemical modeling of fast charge and discharge

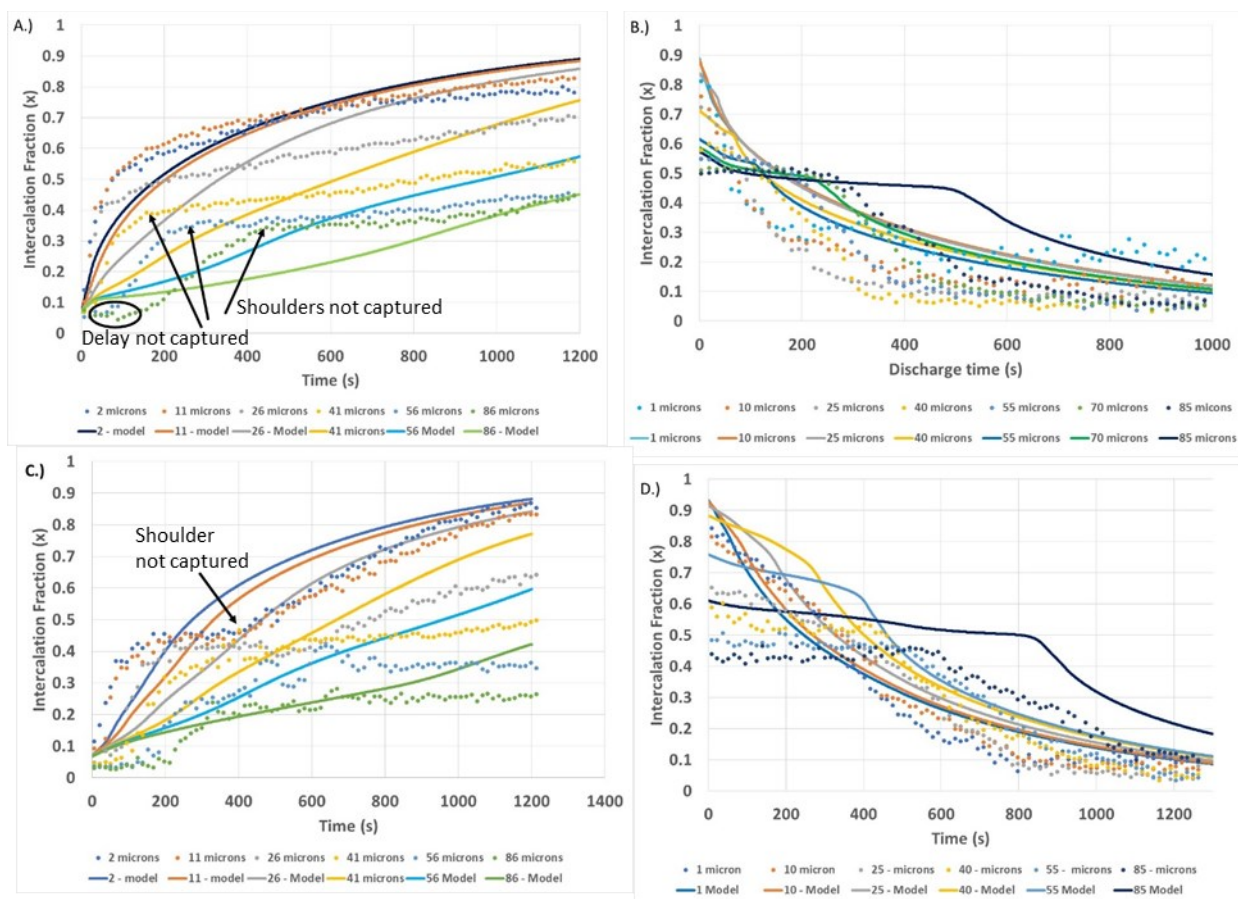
A previously reported electrochemical Newman model is used to simulate fast cycling of the high loading cell and compared with XRD measurements<sup>7, 8</sup>. Parameters for solid-state diffusion and exchange current density of graphite and NMC are reported previously<sup>7</sup>. Electrolyte transport properties are a function of local salt concentration using the equations reported previously<sup>7</sup>. The tortuosity of the anode, cathode, and separator are critical properties for modeling, although they are difficult to measure<sup>7</sup>. The tortuosity of the NMC electrodes with  $\sim 35\%$  porosity is estimated to be around 3 based on microstructure reconstructions, impedance measurements with blocking electrolyte, and electrochemical model fitting to cathode rate data<sup>9</sup>. The separator tortuosity for 2320 has been measured to be around 4<sup>10</sup>. Microstructure reconstructions for graphite anodes with roughly spherical particles and  $\sim 35\%$  porosity is estimated to be around 4. Simulations are run with an initial cell temperature of 25 °C.

Supplementary Figure 9 shows a detailed comparison for XRD measured local intercalation fraction within 100  $\mu\text{m}$  thick graphite versus that predicted from a Newman model. The Newman model captures some features well such as the electrode being preferentially lithiated near the separator during fast charging. Also, during fast discharge the model predicts lithium is first withdrawn near the separator and there is a significant delay in removing lithium from the back half of the electrode. Interestingly during 6C discharge, the XRD measurements and Newman model show the minimum intercalation fraction at modest times is located deep within the

anode. For instance, at 300 s into 6C discharge, the measured minimum is around 40  $\mu\text{m}$  into the anode and the Newman model predicts the minimum is around 50  $\mu\text{m}$ . For 2C discharge, this behavior is not observed or predicted.

The Newman model simulations does miss important features measured via XRD. Some of these are highlighted with arrows and circles in Supplementary Figure 9A and C. For 6C charge, XRD measurements show the back half of the electrode is initially not charged at all. Then after 100-200 s, the back half is rapidly charged to intercalation fractions of 0.3-0.4. Then, the intercalation fraction slowly rises through the remaining charging. This behavior of significant fluctuation in local lithiation rate is not well captured with the Newman model. At 2C discharge, the same behavior is measured, but not captured with the model. Also, at 2C charge the front portion of the electrodes stops lithiating between 100-400 s and this behavior is not captured with the Newman model. At modest discharge times, the XRD measured spread in intercalation fraction is higher than that predicted with a Newman model. Initial attempts to use a solid-state diffusion coefficient for graphite that varies with intercalation fraction did not significantly reduce different between model and XRD measurements.

Initial studies have been performed to investigate whether a more rigorous Chan-Hillard reaction model<sup>11</sup> can capture measured features not predicted with a standard Newman model. The phase-field formulation explicitly considers the thermodynamics of multiple lithium-graphite phases and resolves the moving phase boundaries between phases. Initial results indicate the more rigorous Cahn-Hillard formulation can capture features not predicted by Newman model such as the change in slope of the intercalation fraction near the anode current collector during charging. Both models predict very non-uniform intercalation across the graphite electrode, and a detailed comparison of the different model formulations with XRD data will be the subject of future work. This includes understanding how variations in local intercalation are driven by electrolyte transport limitations vs. staging effects.



Supplementary Figure 9. Intercalation fraction measured within graphite via XRD (dots) vs. Newman model results (lines) for (a) 6C charging, (b) 6C discharging, (c) 2C charging, and (d) 2C discharging. The legend denotes the spatial distance from the graphite/separator interface.

## References

1. A. Missyul, I. Bolshakov and R. Shpanchenko, *Powder Diffraction*, 2017, DOI: doi:10.1017/S0885715617000458, S56-S62.
2. T. J. DiCiccio and B. Efron, *Statist. Sci.*, 1996, **11**, 189-228.
3. B. Efron and R. Tibshirani, *Statist. Sci.*, 1986, **1**.
4. M. Gaurav, B. Haripada, K. B. Pramod and C. Veena, *Journal of Polymer Engineering*, 2014, **34**, 813-821.
5. T. R. Tanim, E. J. Dufek, M. Evans, C. Dickerson, A. N. Jansen, B. J. Polzin, A. R. Dunlop, S. E. Trask, R. Jackman, I. Bloom, Z. Yang and E. Lee, 2019, **166**, A1926-A1938.
6. I. Bloom, A. N. Jansen, D. P. Abraham, J. Knuth, S. A. Jones, V. S. Battaglia and G. L. Henriksen, *Journal of Power Sources*, 2005, **139**, 295-303.
7. A. M. Colclasure, T. R. Tanim, A. N. Jansen, S. E. Trask, A. R. Dunlop, B. J. Polzin, I. Bloom, D. Robertson, L. Flores, M. Evans, E. J. Dufek and K. Smith, *Electrochimica Acta*, 2020, **337**, 135854.

8. A. M. Colclasure, A. R. Dunlop, S. E. Trask, B. J. Polzin, A. N. Jansen and K. Smith, *Journal of The Electrochemical Society*, 2019, **166**, A1412-A1424.
9. F. L. E. Usseglio-Viretta, A. Colclasure, A. N. Mistry, K. P. Y. Claver, F. Pouraghajan, D. P. Finegan, T. M. M. Heenan, D. Abraham, P. P. Mukherjee, D. Wheeler, P. Shearing, S. J. Cooper and K. Smith, *Journal of The Electrochemical Society*, 2018, **165**, A3403-A3426.
10. J. Landesfeind, J. Hattendorff, A. Ehrl, W. A. Wall and H. A. Gasteiger, *Journal of The Electrochemical Society*, 2016, **163**, A1373-A1387.
11. Y. Guo, R. B. Smith, Z. Yu, D. K. Efetov, J. Wang, P. Kim, M. Z. Bazant and L. E. Brus, *The Journal of Physical Chemistry Letters*, 2016, **7**, 2151-2156.